Research Square

Preprints are preliminary reports that have not undergone peer review.
They should not be considered conclusive, used to inform clinical practice,
or referenced by the media as validated information.

Transport Limitations and Defect-Mediated Recombination in Lead- Free Double Perovskite Cs_2AgSbI_6: Implications for Solar-Cell Design

Mohamed Bouzidi
University of Ha'il
Abdullah A. Alatawi
King Abdulaziz City for Science and Technology
Turki Alkathiri
Al-Baha University
Sultan Albarakati
University of Jeddah
Norah Alwadai
Princess Nourah bint Abdulrahman University
Ahmed F. Almutairi
Taibah University
Refka Ghodhbani
Northern Border University
Mohamed Ben Bechir
mohamedbenbechir@hotmail.com
University of Sfax

Article

Keywords: Lead-free double perovskite, Cs_2AgSbI_6, Defect-mediated recombination, Urbach energy, Photoluminescence quenching, SCAPS-1D simulation

Posted Date: April 8th, 2026

DOI: https://doi.org/10.21203/rs.3.rs-9260183/v1

License: This work is licensed under a Creative Commons Attribution 4.0 International License.
Read Full License

Additional Declarations: No competing interests reported.

Transport Limitations and Defect-Mediated Recombination in Lead-Free Double Perovskite Cs_2AgSbI_6: Implications for Solar-Cell Design

Mohamed Bouzidi [1], Abdullah A. Alatawi [2], Turki Alkathiri [3], Sultan Albarakati [4], Norah Alwadai [5], Ahmed F. Almutairi [6], Refka Ghodhbani [7], Mohamed Ben Bechir [8, 9,*]

[1] *Department of Physics, College of Science, University of Ha'il, Ha'il P.O. Box 2440, Saudi Arabia*
[2] *King Abdulaziz City for Science and Technology, P.O. Box 6086, Riyadh 11442, Saudi Arabia*
[3] *Department of Electrical Engineering, College of Engineering, Al-Baha University, Albaha, P.O. Box 65799, Saudi Arabia*
[4] *Department of Physics, College of Science, University of Jeddah, Jeddah, Saudi Arabia*
[5] *Department of Physics, College of Science, Princess Nourah bint Abdulrahman University, P.O. Box 84428, Riyadh 11671, Saudi Arabia*
[6] *Department of Mechanical Engineering, College of Engineering at Yanbu, Taibah University, Yanbu Al-Bahr 41911, Saudi Arabia*
[7] *Center for Scientific Research and Entrepreneurship, Northern Border University, Arar 73213, Saudi Arabia*
[8] *Laboratory of Spectroscopic and Optical Characterization of Materials (LaSCOM), Faculty of Sciences, University of Sfax, Sfax, Tunisia*
[9] *Department of Physics, Faculty of Sciences of Gafsa, University of Gafsa, 2112, Tunisia.*
[*] *Corresponding author. E-mail address: mohamedbenbechir@hotmail.com*

Abstract: Even though the defect-mediated recombination severely limits the photovoltaic performance of lead-free double perovskites, they have become a promising alternative to Pb-based absorbers. The transport mechanisms and the optoelectronic properties of Cs_2AgSbI_6 are systematically investigated in this work by combining impedance analysis, electrical transport, photoluminescence and optical spectroscopy. A highly disordered electronic structure dominated by nonradiative recombination is shown through a non-ideal charge transport, a strong photoluminescence quenching and a large Urbach energy (~90 meV). Based on SCAPS-1D, numerical simulations are carried out using a representative FTO/TiO_2/Cs_2AgSbI_6/Spiro-OMeTAD architecture in order to translate the experimentally observed limitations into a device-level framework. The Shockley–Read–Hall (SRH) recombination is consistently identified by the simulations as the dominant loss pathway, which results in limited photovoltaic parameters and reduced quasi-Fermi level splitting. Defect density is emphasized as the primary bottleneck in Cs_2AgSbI_6-based devices through the strong agreement between numerical trends and experimental material signatures. These results not only offer clear guidelines for defect mitigation strategies towards improved lead-

free perovskite solar cells but also provide device-relevant losses, recombination and a coherent physical picture linking disorder.

Keywords: Lead-free double perovskite; Cs_2AgSbI_6; Defect-mediated recombination; Urbach energy; Photoluminescence quenching; SCAPS-1D simulation

1. Introduction

Owing to the extraordinary optoelectronic properties including defect tolerance, long carrier diffusion lengths and high absorption coefficients, the fast growth of halide perovskite solar cells has made them one of the most promising photovoltaic technologies [1–6]. For Lead-based perovskites, power conversion efficiencies have been reported to exceed 25%, which is close to those of established thin-film technologies [7–10]. In spite of the significant achievements, large-scale commercialization and deployment are severely limited by the concerns regarding long-term stability in addition to the presence of toxic lead [11–13].

Accordingly, the development of lead-free perovskite-inspired materials which has been the focus of considerable research efforts tries to maintain favorable optoelectronic properties while enhancing chemical stability and environmental compatibility [14–16]. Double perovskites with the general formula $A_2BB'X_6$, one of the suggested alternatives, have drawn a lot of attention. Often at the expense of optoelectronic performance, these materials provide reduced toxicity and improved structural robustness when heterovalent cation pairs are substituted for divalent Pb^{2+} [17–20].

Owing to fully inorganic composition, good thermal stability and its suitable band gap for photovoltaic applications, Cs_2AgSbI_6 has become a compelling candidate within this class [21–23]. The basic photovoltaic functionality and the successful thin-film fabrication in Cs_2AgSbI_6-based devices have been proven in several experimental studies. However, the underlying physical mechanisms which limit the device performance are not grasped entirely and the reported power conversion efficiencies are still modest [21, 24].

The presence of strong electronic disorder shown by pronounced photoluminescence quenching, broad sub-bandgap absorption tails and large Urbach energies is a recurring feature in both Cs_2AgSbI_6 and related lead-free double perovskites. The defect-assisted nonradiative recombination which plays a key part in dominating carrier dynamics is strongly implied by these observations. Double perovskites tend to show reduced carrier lifetimes and deeper defect states, which leads to low open-circuit voltages and limited quasi-Fermi level splitting, unlike lead-based perovskites where defect tolerance frequently mitigates recombination losses [21, 24, 25].

A quantitative and clear relationship between the photovoltaic performance, the recombination mechanisms and the material disorder in Cs_2AgSbI_6 devices is still missing even though the number of experimental reports is increasing [21, 24, 25]. Multiple studies, indeed, report optical and electrical measurements that do not offer a unified physical framework allowing the identification of the dominant loss channels. Numerical device simulations can give important insight into these mechanisms as soon as they are cautiously constrained by experimental observations. These simulations, however, show the intrinsic material limitations observed experimentally and necessarily avoid idealized assumptions.

To analyze energy band alignment, recombination and charge transport in thin-film solar cells, SCAPS-1D numerical simulations are found to be a powerful tool in this regard [26]. SCAPS enables a realistic assessment of bulk- and interface-limited processes when combined with experimentally derived parameters, which makes a direct comparison with photophysical signatures and measured current–voltage characteristics possible [27-30].

A combined numerical and experimental investigation of Cs_2AgSbI_6-based solar cells is shown in this paper. The electrical, optical and structural characteristics of the absorber layer analyzed experimentally reflect non-ideal transport behavior and strong disorder-induced recombination. Therefore, these findings are employed so as to construct a physically-constrained SCAPS-1D model where carrier losses are governed by the SRH recombination, which is in agreement with large Urbach energies and photoluminescence quenching.

The simulations reproduce the behaviors experimentally noticed in the fill factor, the short-circuit current density and the open-circuit voltage by systematically varying the defect density in the absorber layer. Additionally, spatially-resolved profiles of recombination, generation, quasi-Fermi level splitting and carrier density present evidence that the primary performance bottleneck in Cs_2AgSbI_6 devices is the bulk defect-mediated recombination.

This combined approach makes it possible to move not only towards a mechanistic understanding of performance limitations in lead-free double perovskite solar cells but also beyond purely descriptive experimental observations. The results highlight interface engineering and defect passivation as essential strategies for future improvement and rationalize the current efficiency ceiling of Cs_2AgSbI_6 devices.

2. Experimental Section

Materials: Cesium iodide (CsI, Sigma-Aldrich, 99.9%), silver bromide (AgBr, Sigma-Aldrich, 99.99%), antimony(III) bromide ($SbBr_3$, Sigma-Aldrich, 99.999% trace metals basis), trimethylsilyl iodide (TMS-I, Sigma-Aldrich, ≥98%), octadecene (ODE, Sigma-Aldrich, 90%),

oleic acid (OA, Sigma-Aldrich, 90%) and oleylamine (OLAm, Sigma-Aldrich, 70%) were used as received without further purification.

Synthesis: Cs_2AgSbI_6 required a post-synthetic anion-exchange route and could not be obtained by direct synthesis due to the thermodynamic preference of the layered $Cs_3Sb_2I_9$ phase under iodide-rich conditions [25].

Using a solution-based synthesis, $Cs_2AgSbBr_6$ was first prepared under inert atmosphere. Stoichiometric amounts of the antimony, silver and cesium precursors were heated under controlled conditions after being dissolved in a mixture of oleylamine, oleic acid and octadecene. To promote phase formation, the reaction temperature was raised to 180 °C after degassing at 110 °C. Then, the reaction was rapidly quenched. The resulting material was purified by centrifugation after repeated washing.

Later, Cs_2AgSbI_6 was obtained via halide exchange through the introduction of trimethylsilyl iodide into a dispersion of the $Cs_2AgSbBr_6$ material under inert conditions at room temperature. In order to ensure the complete substitution of bromide by iodide, the exchange reaction was left to continue for almost one hour. Before the fabrication of the device, the resulting Cs_2AgSbI_6 material was collected, dried and stored under inert atmosphere.

While suppressing the formation of the layered $Cs_3Sb_2I_9$ structure, the stabilization of the three-dimensional iodide double-perovskite phase was enabled by the two-step approach.

Characterizations: Using a PANalytical Empyrean diffractometer equipped with Cu Kα radiation (λ = 1.5406 Å), the Powder X-ray diffraction (XRD) measurements were conducted at 30 mA and 40 kV. The diffraction patterns were recorded in the Bragg angle range 2θ = 10–50° with a 0.05° step size at room temperature.

To assess structural parameters and phase purity and also identify the crystalline phase, the collected diffraction data were analyzed. Using the CELREF software (version 3), the lattice-parameter refinement and indexing were carried out assuming a cubic symmetry. The fitting quality and refined structural parameters were evaluated through minimizing the difference between calculated and observed peak positions.

By means of a Shimadzu UV-2550 spectrophotometer equipped with a diffuse reflectance accessory, diffuse reflectance optical measurements were conducted at room temperature. While $BaSO_4$ was employed as the reflectance reference standard, the polycrystalline Cs_2AgSbI_6 powder samples were gently pressed and mounted in the sample holder.

Over the wavelength range 300–800 nm which corresponds to photon energy range 1.5–4.15 eV, diffuse reflectance spectra were collected with a spectral resolution of about 0.01 eV. The

measured reflectance data R(λ) were converted into the Kubelka–Munk function which is proportional to the optical absorption coefficient for optically-thick samples. Later, assuming direct and indirect allowed transitions, optical bandgap energies were calculated through Tauc analysis based on the Kubelka–Munk formalism.

Using a Shimadzu RF-1501 spectrofluorometer, Steady-state photoluminescence (PL) measurements were carried out. Providing photon energies well above the optical absorption edge of Cs_2AgSbI_6 so as to ensure an efficient photocarrier generation, the excitation wavelength was fixed at 405 nm (3.06 eV).

To minimize parasitic background signals and scattering effects, polycrystalline powder samples were gently pressed and mounted on a non-luminescent sample holder. With a spectral resolution of approximately 2 meV, PL spectra were recorded in the photon-energy range 0.75–1.55 eV.

Using a temperature-controlled cryogenic stage, temperature-dependent PL measurements were carried out in the temperature range 70–300 K. Thermal equilibrium was ensured at each temperature before data acquisition. The spectra recorded were corrected for the instrumental response of the detection system. To subtract detector background and electronic noise, dark spectra recorded in the absence of optical excitation were employed, which guarantees that the intrinsic photoluminescence of the material is the exclusive source of the extracted emission features.

Using a Keithley 2400 SourceMeter performing in a source-voltage mode, current–voltage (I–V) measurements were conducted at room temperature. With a diameter of 8 mm, the polycrystalline Cs_2AgSbI_6 samples were pressed into circular pellets. By means of conductive electrodes applied to opposite faces of the pellet, these samples were contacted in a two-probe configuration.

While the resulting current was recorded with high sensitivity, the applied voltage was swept symmetrically between positive and negative bias values. To minimize capacitive effects and ensure steady-state conditions, an appropriate delay time was applied at each voltage step.

To begin with, Dark I–V properties were measured in the absence of optical excitation. Using identical voltage sweep conditions, illuminated I–V measurements were later carried out under continuous optical illumination. Many measurement cycles were conducted not only to exclude transient or irreversible effects but also to verify reproducibility.

By means of a Zahner electrochemical workstation, impedance spectroscopy (IS) measurements were carried out over a frequency ranging from 1.3551 Hz to 1×10^7 Hz on pelletized Cs_2AgSbI_6 samples with an 8-mm diameter.

At room temperature, impedance spectra were recorded under both illuminated and dark conditions. In addition, to investigate thermally-activated charge-transport processes, temperature-dependent IS measurements were performed over temperature ranging from 303 to 378 K under dark conditions. Before data acquisition, the sample was allowed to reach thermal equilibrium at each temperature.

Via ZView software, the collected impedance data were analyzed by fitting the experimental spectra with appropriate equivalent electrical circuits consisting of constant phase elements (CPEs) and resistive elements. This modeling approach offers a quantitative description of the charge-transport mechanisms dominating polycrystalline Cs_2AgSbI_6, accounts for the non-ideal capacitive behavior originating from structural disorder and makes the separation of grain-boundary and bulk (grain) contributions possible.

3. Results and discussion

3.1. Crystal structure and phase purity of polycrystalline Cs_2AgSbI_6

The XRD pattern of the polycrystalline Cs_2AgSbI_6 compound at room temperature is recorded through Cu Kα radiation (λ = 1.5406 Å) in the 2θ range of 10–50° as displayed in Fig. 1(a). The diffractogram shows a set of well-defined and sharp diffraction peaks, which confirms not only the absence of any significant amorphous contribution but also the good crystallinity. The (002), (022), (222), (004), (402) and (044) crystallographic planes indicative of a three-dimensional double-perovskite structure can be linked to the main reflections observed at 2θ ≈ 14.38°, 20.41°, 25.05°, 29.03°, 32.53° and 41.50° respectively. The formation of a single-phase Cs_2AgSbI_6 compound is demonstrated since no additional peaks connected to secondary phases including $Cs_3Sb_2I_9$, AgI or other iodide by-products are detected in the instrumental resolution [25].

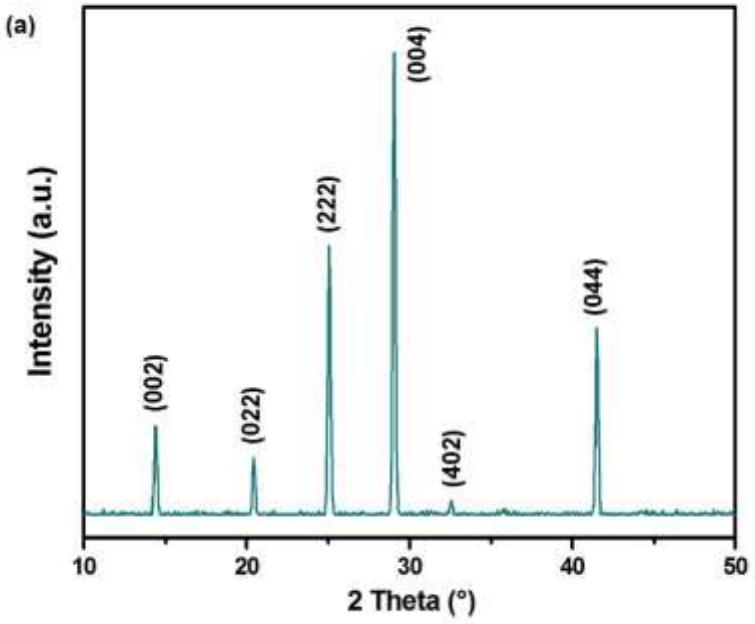
A cubic symmetry is assumed by the lattice-parameter refinement and indexing conducted using CELREF (version 3) [26]. Fig. S1 displays the peak matching and the refinement procedure. A unit-cell volume of V=1860.83 $Å^3$ matches the refined lattice parameters obtained from the CELREF output which are: a = b = c = 12.2999 ± 0.0040 Å, α = β = γ = 90°. Added to the low root-mean-square deviation $\sqrt{\sum \frac{(2\theta_{obs}-2\theta_{calc})^2}{N_{ref}-N_{par}}} = 0.0091$, the slight differences between calculated and observed peak positions (|Δ2θ| < 0.04°) indicate not only the validity of the cubic structural model but also the excellent quality of the refinement.

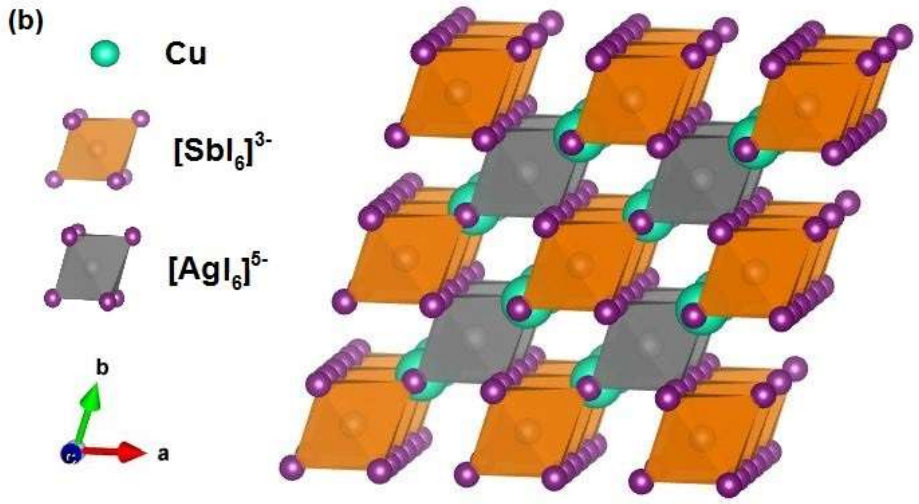
The refined lattice parameter corresponds well to the values reported in recent literature. For the Cs_2AgSbI_6 synthesized via halide exchange, a cubic lattice parameter close to 12.02 Å was indeed reported by Horani and Gamelin. As for the iodide member of the Cs_2AgSbX_6 (X = Cl,

Br, I) family, a cubic lattice constant of nearly 12.3 Å is predicted by first-principles calculations [25]. Contrary to nanocrystalline systems, the microstrain and the defect effects inherent to solid-state synthesis in addition to the bulk polycrystalline nature of the sample are possibly the reasons why the value obtained in our study is slightly larger.

Using the VESTA visualization software [27], the corresponding crystal structure is shown in Fig. 1(b). Corner-sharing $[AgI_6]^{5-}$ and $[SbI_6]^{3-}$ octahedra alternate in a rock-salt arrangement throughout the lattice in a three-dimensional elpasolite-type double perovskite structure where Cs_2AgSbI_6 crystallizes. The electrostatic stabilization of the structure is ensured by the Cs^+ cations occupying the A-sites of the perovskite framework. Cs_2AgSbI_6 is distinguished from lower-dimensional iodide antimonates (for example $Cs_3Sb_2I_9$ adopting quasi-two-dimensional or layered structures) through the continuous three-dimensional octahedral connectivity [24, 25].

The key result is the unambiguous identification of a cubic three-dimensional double-perovskite structure, which offers the structural foundation for the recombination, transport and optical properties discussed in the following sections. More importantly, the bulk-dominated charge-transport behavior, the defect-related electronic states and the observed optical absorption characteristics of polycrystalline Cs_2AgSbI_6 are directly underpinned by the presence of a 3D corner-sharing network.





Figs. 1. (a) X-ray diffraction pattern of polycrystalline Cs_2AgSbI_6 recorded at room temperature. (b) Crystal structure of cubic Cs_2AgSbI_6 visualized using VESTA software.

3.2. Diffuse reflectance spectroscopy and disorder-induced band-edge states

By means of UV–visible diffuse reflectance spectroscopy, the optical response of polycrystalline Cs_2AgSbI_6 has been studied to probe its intrinsic absorption properties in a bulk-relevant configuration. A gradual decline with growing photon energy without a sharp absorption onset is proven by the diffuse reflectance spectrum shown in Fig. 2(a), which confirms a broadened band-edge absorption. This behavior represents polycrystalline lead-free double perovskites where localized electronic states are introduced near the band edges by point defects, grain boundaries and structural disorder.

The diffuse reflectance data were converted to quantitatively analyze the optical absorption using the Kubelka–Munk formalism [33]:

$$F(R) = \frac{(1-R)^2}{2R} \quad (1)$$

where R stands for the measured diffuse reflectance. Standard bandgap analyses are allowed to be applied since F(R) is proportional to the absorption coefficient α for optically thick samples.

As displayed in Fig. 2(b), an indirect allowed transition is assumed by the nature of the fundamental optical transition which was examined using Tauc analysis as follows [34]:

$$(F(R)h\nu)^{1/2} = A\left(h\nu - E_g^{idn}\right) \quad (2)$$

where hν refers to the photon energy, A represents a proportionality constant, and E_g^{idn} is the indirect bandgap. Immediately above the absorption edge, a well-defined quasi-linear region is noticed. An apparent indirect bandgap of E_g^{idn} = 1.65 ± 0.05 eV which is yielded by the linear extrapolation of this region to zero absorption is typical of an effective bulk optical gap rather affected by disorder-induced band tailing than by a strict intrinsic bandgap of an ideal crystal. The influence of band-tail states and the finite width of the transition region which

slightly modify the exact position of the linear onset are reflected by such uncertainty. Therefore, the extracted value is a distinction that is particularly relevant in disordered polycrystalline systems as it is not typical of a perfectly ideal band edge but it rather represents an effective absorption threshold.

As shown in Fig. 2(c), the absorption behavior was further analyzed at higher photon energies, assuming a direct allowed transition described by the following equation:

$$(F(R)h\nu)^2 = B\left(h\nu - E_g^{dir}\right) \quad (3)$$

where B represents a proportionality constant while E_g^{dir} refers to the direct transition energy. In this case, a linear region does not emerge for the indirect transition but rather appears at higher energies. In contrast, its exact slope and intercept depend sensitively on the selected fitting window. Such sensitivity originates from the possible overlap of multiple interband transitions in the high-energy region and the intrinsic broadening of the absorption edge. Consequently, due to the intrinsic broadening of the absorption edge, the direct transition energy should be regarded as indicative rather than definitive and is reported as E_g^{dir} = 2.66 ± 0.1 eV. This uncertainty is not experimental noise but a physical manifestation of the disorder-induced broadening and the complex electronic structure in the polycrystalline material.

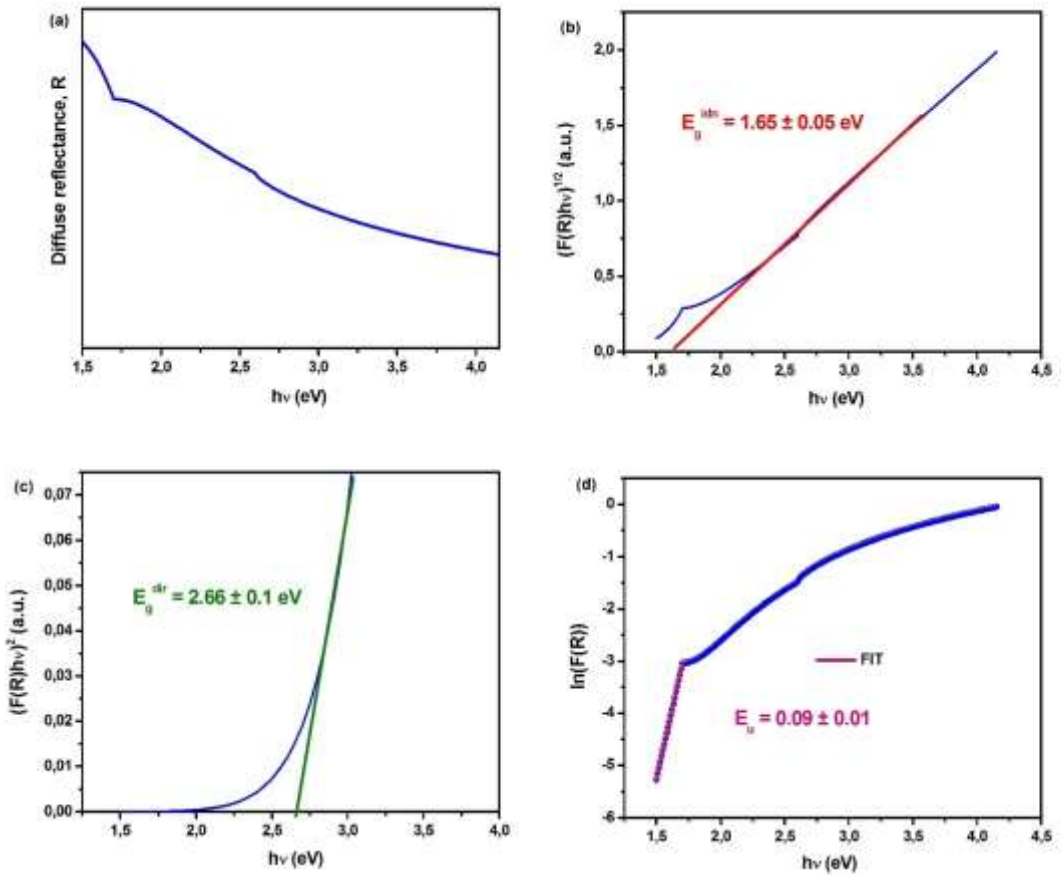
Through Urbach analysis which captures the contribution of localized states associated with structural disorder, the exponential absorption tail below the band edge was quantified. As displayed in Fig. 2(d), the Urbach relation can be written as follows [35]:

$$\alpha(h\nu) = \alpha_0 \exp\left(\frac{h\nu}{E_u}\right) \quad (4)$$

or equivalently using the Kubelka–Munk function [36]:

$$ln[F(R)] = \frac{h\nu}{E_u} + C \quad (5)$$

where E_u stands for the Urbach energy while C represents a constant. A clear linear region from which an Urbach energy of E_u = 0.09 ± 0.01 eV is extracted is observed in the sub-bandgap regime of the ln[F(R)] as a function of hν plot. A substantial density of localized states extending into the bandgap which originates from defect-related disorder, compositional fluctuations and lattice distortions is confirmed by the relatively large Urbach energy. The strong linearity of the Urbach region which is generally less sensitive to fitting-window selection than the direct transition analysis is reflected by the small uncertainty associated with E_u.



Figs. 2. (a) UV–visible diffuse reflectance spectrum of polycrystalline Cs_2AgSbI_6. (b) Tauc plot for the indirect allowed transition derived from the Kubelka–Munk function. (c) Tauc plot for the direct allowed transition at higher photon energies. (d) Urbach plot extracted from diffuse reflectance data for the determination of the Urbach energy.

A coherent picture of the electronic structure of polycrystalline Cs_2AgSbI_6 is revealed by the optical absorption analysis taken as a whole (Figs. 2(a)-(d)). The interaction between the extrinsic disorder effects introduced by the polycrystalline morphology and the intrinsic band structure of the double perovskite lattice is highlighted by the combination of a pronounced Urbach tail, a higher-energy direct transition and a reduced apparent indirect bandgap. The present bulk material shows enhanced band-tail states that significantly influence its optical absorption in comparison with more idealized or highly-ordered systems where smaller Urbach energies and sharper absorption onsets are typically observed. This broadened absorption landscape facilitates enhanced photocarrier generation and sub-bandgap optical excitation, which are beneficial for not only optoelectronic applications requiring stable lead-free materials but also broadband photodetection rather than represents a disadvantage.

3.3. Photoluminescence and temperature-dependent recombination mechanisms

In order to elucidate the nature of radiative recombination processes and their relationship with the disorder-induced electronic states shown by optical absorption, the photoluminescence properties of polycrystalline Cs_2AgSbI_6 were investigated. The steady-

state PL spectra recorded under fixed excitation conditions over the temperature range of 70–300 K are displayed in Fig. 3(a) [37, 38]. The PL intensity progressively declines upon increasing temperature and becomes significantly quenched at room temperature, whereas a broad emission band centered in the near-infrared region is clearly observed at low temperature.

The absence of sharp excitonic features and the broad spectral profile show that the emission originates from recombination involving localized states and is not governed by free band-to-band recombination [39, 40]. This behavior not only reflects the defect landscape of the polycrystalline material and the intrinsic structural disorder but is also consistent with the presence of band-tail states inferred from the Urbach analysis [41]. Using a Gaussian-based model, each PL spectrum was fitted so as to quantitatively analyze the emission features, which makes reliable extraction of peak position and linewidth possible. The spectral intensity was described as follows [42, 43]:

$$I(E) = A\ exp\left[-\frac{(E-E_{peak})^2}{2\sigma^2}\right] + C \quad (6)$$

where A is the amplitude, E_{peak} refers to the peak emission energy, σ represents the standard deviation related to the spectral broadening and C accounts for a residual background contribution. The full width at half maximum (FWHM) was obtained from $FWHM = 2\sqrt{2ln2}\sigma$ [44, 45]. Table 1 summarizes the extracted fitting parameters, including not only FWHM and E_{peak} but also their uncertainties.

Table 1. Photoluminescence fitting parameters of polycrystalline Cs_2AgSbI_6 obtained from Gaussian analysis.

T (K)	E_{peak} (eV)	E_{peak} uncertainty (eV)	FWHM (eV)	FWHM uncertainty (eV)	R^2 (fit quality)
70	1.0836	±0.0021	0.4074	±0.0035	0.9994
100	1.0813	±0.0020	0.4247	±0.0035	0.9994
130	1.0928	±0.0016	0.4277	±0.0032	0.9993
160	1.1122	±0.0010	0.4199	±0.0025	0.9993
200	1.1252	±0.0006	0.4203	±0.0015	0.9997
250	1.1221	±0.0027	0.4420	±0.0069	0.9966
300	1.1111	±0.0028	0.4786	±0.0106	0.9876

Fig. 3(b) displays the temperature dependence of the integrated PL intensity obtained by numerical integration of the fitted spectra. As soon as the temperature rises, the PL intensity decreases rapidly, which confirms the strong thermal quenching of radiative recombination

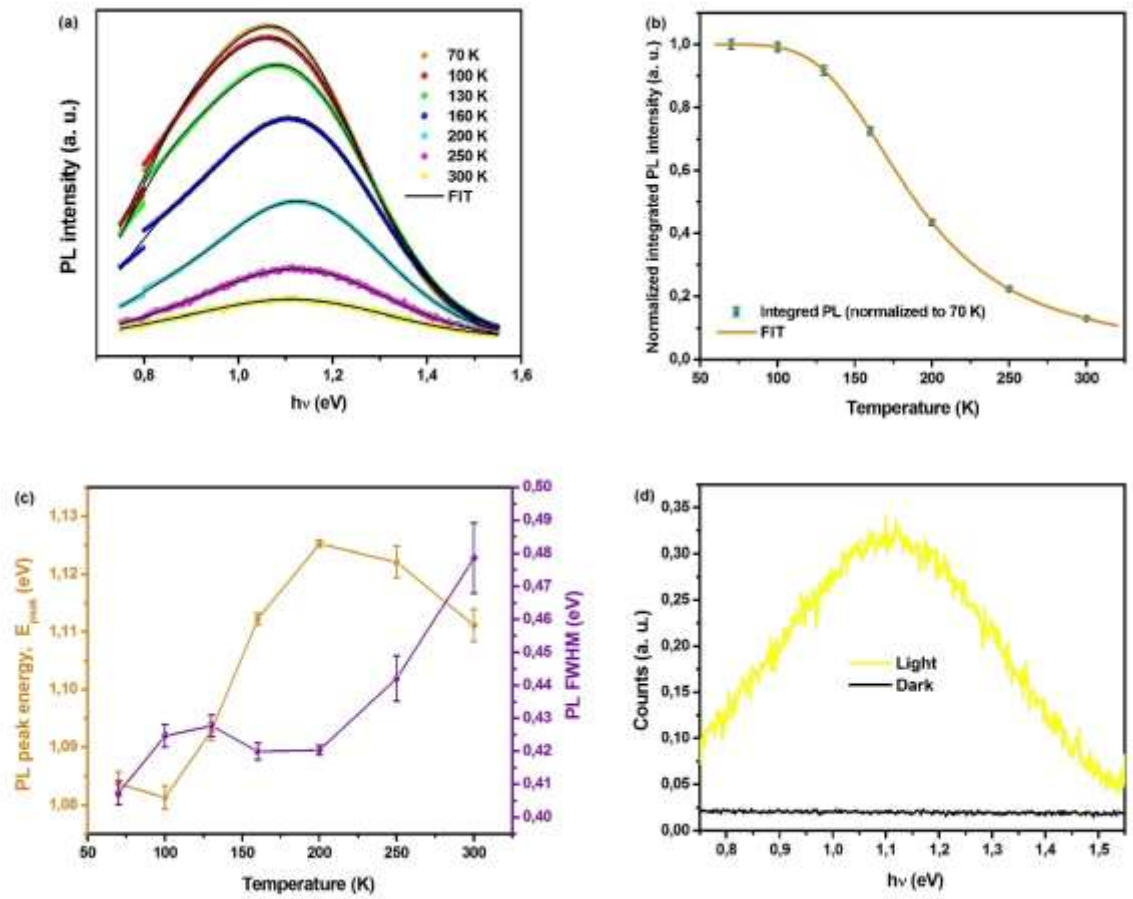
[46]. Using a thermally activated nonradiative recombination model, this behavior was analyzed as follows [47]:

$$\frac{I(T)}{I_0} = \frac{1}{1+A\exp\left(-\frac{E_a}{k_B T}\right)} \quad (7)$$

where I(T) is the integrated PL intensity at temperature T, I_0 denotes the low-temperature reference intensity, A represents a pre-exponential factor, E_a refers to the activation energy associated with nonradiative recombination channels and k_B stands for the Boltzmann constant. An activation energy of nearly $E_a \approx 0.085$ eV is yielded by fitting the experimental data, which suggests that, when thermal energy goes up, nonradiative recombination is efficiently mediated by relatively shallow defect states [48]. Most importantly, a common physical origin associated with shallow disorder-induced states is implied by the fact that this activation energy is comparable to the Urbach energy extracted from absorption measurements.

Based on the fitting parameters reported in Table 1, Fig. 3(c) depicts the evolution of the spectral width and the PL peak energy with temperature. With increasing temperature, the FWHM reveals a moderate broadening, whereas the emission peak shows only a weak temperature dependence within experimental uncertainty. This behavior does not reflect conventional bandgap renormalization typically observed in highly-ordered crystalline semiconductors. Instead, it demonstrates not only thermal population of a wider distribution of localized states but also enhanced electron–phonon interactions at elevated temperatures [49]. Rather than free excitonic transitions, the assignment of the PL emission to self-trapped or defect-related carrier recombination is further supported by the absence of a pronounced monotonic shift.

PL spectra acquired not only in the absence of excitation (“dark”) but also under illumination (“light”) are compared in Fig. 3(d) so as to further validate the intrinsic nature of the observed emission at room temperature. Only the electronic noise and the detector background are revealed by the dark spectrum while a weak but reproducible PL signal is reflected by the subtraction of this contribution from the illuminated spectrum. Such analysis demonstrates that, despite the strong thermal quenching evidenced in Fig. 3(b), the residual emission observed at room temperature is not an instrumental artifact but it arises from the material itself.



Figs. 3. (a) Steady-state photoluminescence spectra of polycrystalline Cs_2AgSbI_6 recorded over the temperature range 70–300 K. (b) Temperature dependence of the integrated photoluminescence intensity. (c) Temperature dependence of photoluminescence peak energy and full width at half maximum. (d) Photoluminescence spectra under illumination and dark conditions at room temperature.

A coherent picture of recombination in polycrystalline Cs_2AgSbI_6 is generally provided by the PL results. Rather than band-edge excitonic processes, localized states associated with defects and structural disorder govern radiative recombination, which is implied by the limited temperature dependence of the peak energy, the strong thermal quenching and the broad emission. Such findings completely agree with both the large Urbach energy and the broadened absorption edge extracted from diffuse reflectance measurements. Notably, at room temperature, the predominance of nonradiative recombination justifies the use of defect-assisted SRH recombination models in the subsequent SCAPS simulations where, instead of radiative lifetimes, defect states primarily dominate device-relevant behavior and carrier transport.

3.4. Electrical transport and photoconductive behavior

Through I–V measurements performed under illuminated and dark conditions, the electrical transport properties of polycrystalline Cs_2AgSbI_6 shown in Fig. 4(a) were investigated at room temperature. Without pronounced rectification or diode-like behavior, a nearly symmetric and smooth response with respect to voltage polarity is displayed by The I–V characteristics. This

implies that charge transport is dominated by bulk conduction through a polycrystalline network where defect states and grain boundaries play a key role rather than by a single depletion junction.

As shown in the zoomed representation in Fig. 4(b), the dark I–V characteristics were analyzed in the low-bias region ($|V| \leq 0.2$ V) so as to quantitatively identify the transport regime at low electric fields. In this regime, the current varies linearly with the applied voltage and can be described by the following ohmic relation [50]:

$$I = b + GV \tag{8}$$

where G=dI/dV stands for the conductance while b represents a small offset current. A linear fit of the experimental data yields as follows:

$$G = 8.49 \times 10^{-6} A\, V^{-1}, \qquad b = 2.05 \times 10^{-9} A$$

Compared to the measured current levels, the intercept b is negligible, which confirms the rectifying effects at low bias or the absence of significant built-in currents. Therefore, the corresponding effective resistance is as follows [51]:

$$R_{eff} = \frac{1}{G} \approx 1.18 \times 10^{5} \Omega \ (\sim 118\, k\Omega) \tag{9}$$

An ohmic transport regime is unambiguously confirmed at low electric fields by the high correlation coefficient obtained from the fit (R = 0.994, N = 9, P < 0.0001). Such behavior shows charge transport through percolative paths formed by interconnected grains in which defect-assisted scattering, rather than injection barriers at the contacts, limits carrier motion.

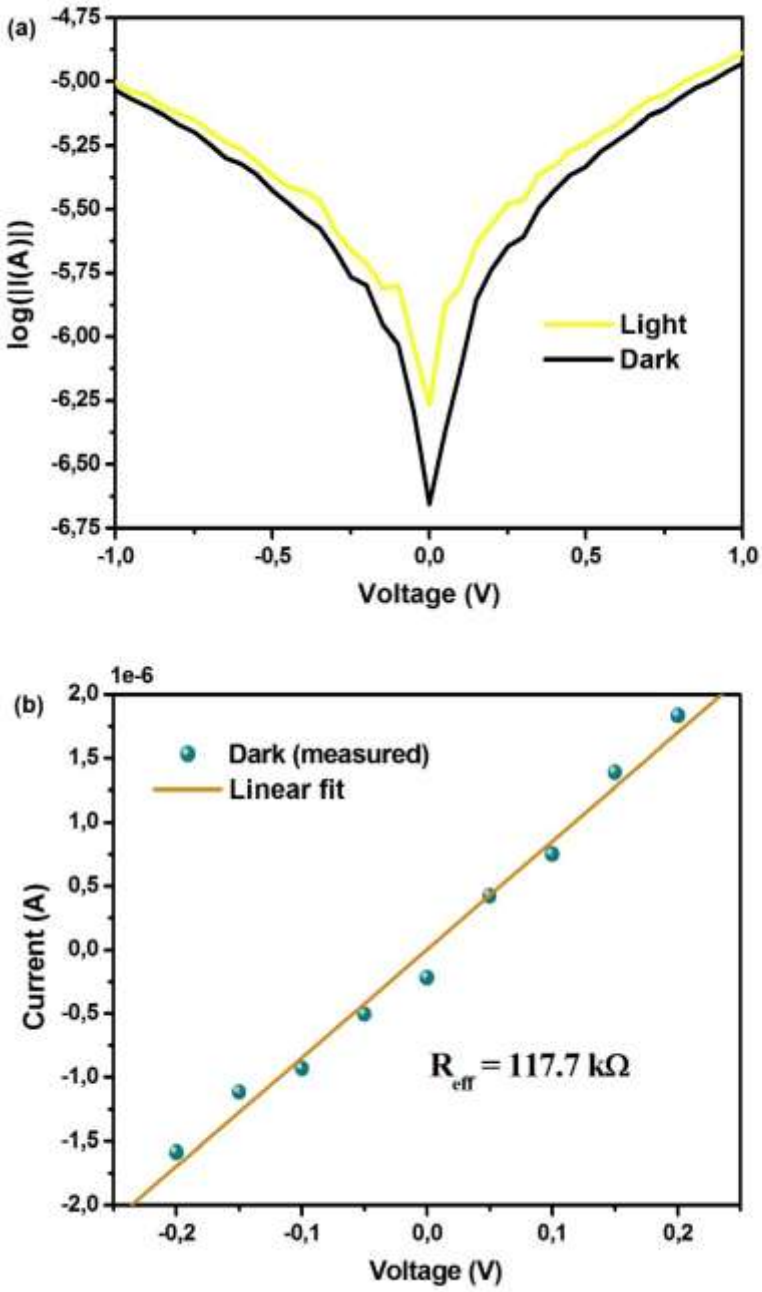
The increasing influence of field-assisted transport mechanisms is confirmed as a gradual deviation from perfect linearity is displayed by the I–V characteristics at higher applied voltages [52]. This behavior is indicative of field-assisted and trap-controlled transport and is commonly observed in polycrystalline and disordered semiconductors [53]. Instead of space-charge-limited current in a well-defined single-crystal channel, distributed bulk and grain-boundary effects still govern transport, which is suggested by the absence of sharp nonlinearities or abrupt transitions.

A clear photoconductive effect is demonstrated since, compared to the dark response, a systematic increase in current magnitude is shown in Fig. 4(a) under optical illumination over the entire voltage range by the I–V curves. The illuminated current can be expressed as follows [54]:

$$I_{light}(V) = I_{dark}(V) + I_{ph}(V) \tag{10}$$

where I_{ph} stands for the photocurrent contribution originating from photogenerated carriers. The fact that the photocarrier extraction and generation do not take place within a narrow

depletion region but rather throughout the bulk of the material is confirmed by the persistence of a finite photocurrent for negative and positive bias polarities.



Figs. 4. (a) Current–voltage characteristics of polycrystalline Cs_2AgSbI_6 measured under dark and illuminated conditions at room temperature. (b) Low-bias current–voltage response and linear fitting of the ohmic regime.

Observed between negative and positive bias under illumination, the modest asymmetry can be attributed to not only internal electric fields associated with spatially inhomogeneous defect distributions and grain boundaries but also to non-identical electrical contacts [55]. Notably, under illumination, the absence of strong rectification demonstrates that carrier

extraction is controlled by recombination processes and bulk transport instead of Schottky barriers.

The I–V transport behavior completely agrees with the photoluminescence and optical absorption results previously discussed. With an activation energy of $E_a \approx 0.085$ eV, the strong thermal quenching of photoluminescence indicates efficient nonradiative recombination via shallow defect states, whereas the large Urbach energy ($E_u = 0.09 \pm 0.01$ eV) shows a high density of localized states near the band edges. Such defect states simultaneously dominate charge transport, radiative recombination and optical absorption.

The fact that the charge transport in polycrystalline Cs_2AgSbI_6 is governed not only by grain-boundary conduction but also by defect-assisted bulk is unambiguously demonstrated by the photoconductive behavior, the impedance-derived activation energies and the linear low-field I–V response as a whole.

For the SCAPS simulations presented below where recombination and charge transport are modeled using defect-assisted SRH mechanisms [56], the parameters that are determined experimentally form a consistent and physically grounded basis, which is in direct accordance with the electrical, optical and photoluminescence measurements.

3.5. Impedance spectroscopy and thermally activated charge transport

Impedance spectroscopy was used not only to disentangle the respective contributions of grains and grain boundaries in addition to their evolution with optical illumination and temperature but also to better understand the charge-transport mechanisms in polycrystalline Cs_2AgSbI_6. The Nyquist plots ($-Z''$ versus Z') recorded over the temperature range 303–378 K in the dark are displayed in Fig. 5(a). A thermally activated reduction in the resistive components is confirmed by the spectra that consist of depressed semicircular arcs whose overall diameter declines markedly as soon as the temperature rises [57]. Due to photogenerated charge carriers, an increase in electrical conductivity is proven by the inset of Fig. 5(a) that compares the Nyquist responses measured at 303 K under dark and illuminated conditions where illumination leads to a systematic shrinkage of the arcs [57].

Using an equivalent circuit composed of two parallel (R‖CPE) elements connected in series, followed by an additional CPE accounting for low-frequency polarization effects [58], the impedance data were fitted to quantitatively analyze these spectra. The deviations from ideal capacitive behavior originate from a distribution of relaxation times and structural disorder while the circuit is well suited to polycrystalline semiconductors where transport is dominated by not only grain-boundary barriers but also bulk (grain) conduction. The impedance of a constant phase element (CPE) is expressed as follows [57]:

$$Z_{CPE} = \frac{1}{Q(jw)^{\alpha}} \quad (11)$$

where Q represents the pseudo-capacitance, ω stands for the angular frequency and $0 < \alpha \leq 1$ describes the degree of non-ideality. The impedance can be written as follows for a parallel (R‖CPE) branch:

$$Z_{R\|CPE} = \frac{R}{1+RQ(jw)^{\alpha}} \quad (12)$$

For the dark spectrum at 303 K, Fig. S2 shows an example of the fitting quality that indicates excellent agreement between the simulated response obtained using ZView and the experimental data. Table 2 provides a summary of the full set of fitted parameters extracted for all illumination conditions and temperatures. The grain-boundary resistance, $R_{gb} \sim 2.7 \times 10^6\ \Omega$, is significantly larger than the resistance associated with the grains in the dark at 303 K which is on the order of $R_g \sim 2.0 \times 10^5\ \Omega$, indicating that grain-boundary barriers associated with defect-rich intergranular regions predominantly limit charge transport [57, 58]. At grain boundaries, a stronger non-ideal behavior which is consistent with a higher density of localized states in these regions and enhanced disorder is confirmed by the corresponding CPE exponents ($\alpha_{gb} \approx 0.8$ for grain boundaries and $\alpha_g \approx 0.9$ for grains).

The associated CPE exponents remain nearly unchanged, whereas both R_g and R_{gb} decline by approximately 10–15% under illumination at 303 K. Such observation demonstrates that the density of mobile carriers primarily increases owing to light. Thus, without altering the fundamental transport mechanisms, the resistive components is reduced. This behavior supports a bulk-dominated photogeneration process rather than interface-limited carrier extraction and is fully consistent with the photoconductive response observed in the I–V measurements.

The temperature dependence of the fitted resistances follows an Arrhenius-type behavior described by:

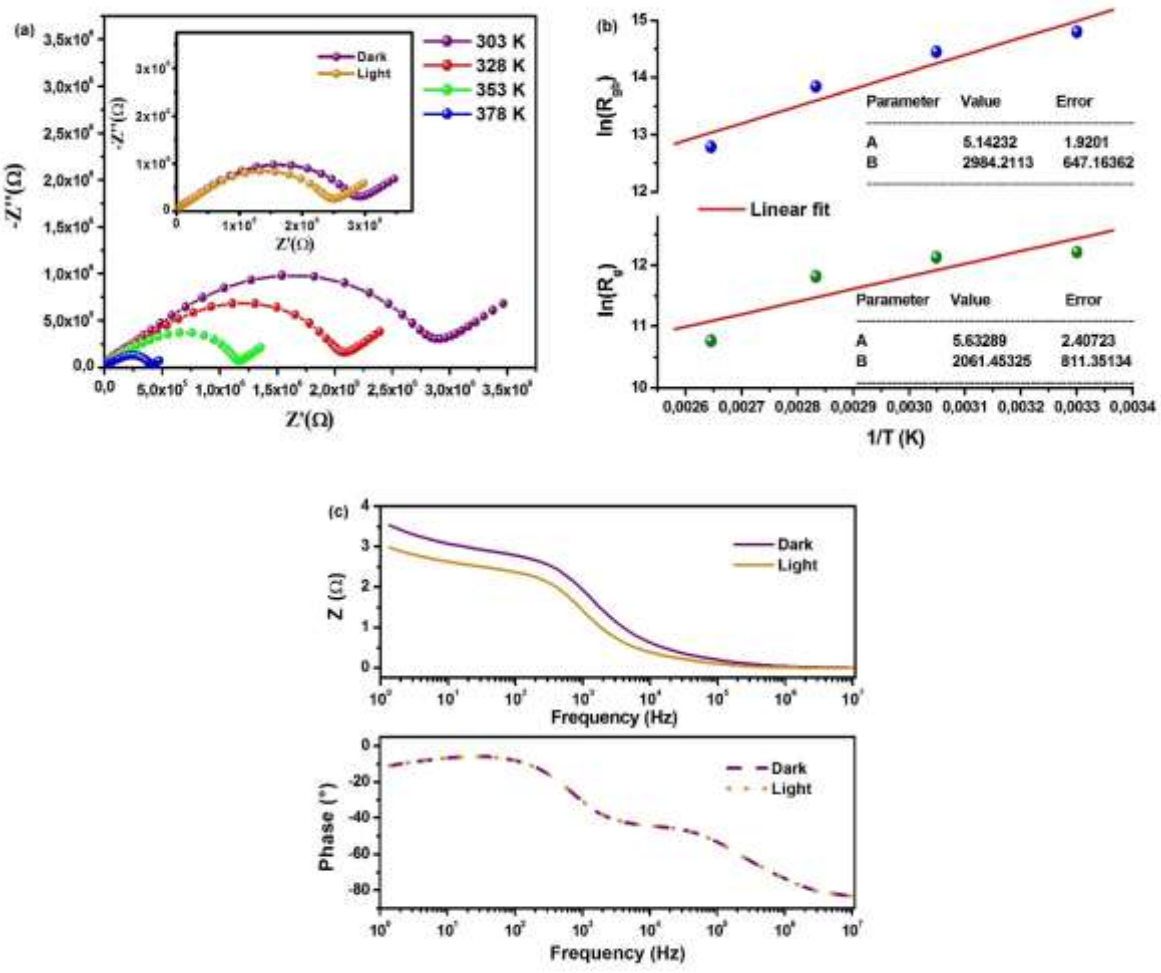
$$R(T) = R_0 \exp\left(\frac{E_a}{k_\beta T}\right), \text{ or equivalently } lnR = lnR_0 + \frac{E_a}{k_\beta}\frac{1}{T}, \quad (13)$$

where E_a stands for the activation energy associated with charge transport.

The plots of $\ln(R_g)$ and $\ln(R_{gb})$ as a function of 1/T are displayed in Fig. 5(b). Linear fits yield activation energies of $E_a(R_{gb}) = 0.25716$ eV for the grain-boundary contribution and $E_a(R_g) = 0.17764$ eV for the grain (bulk) contribution. Compared to the grain interiors, these regions present deeper trap distributions and larger potential barriers due to the higher activation energy associated with grain boundaries.

Table 2. Impedance fitting parameters of polycrystalline Cs_2AgSbI_6 obtained from equivalent circuit analysis.

Condition	*T (K)*	R_g (Ω)	C_g (F)	α_g	R_{gb} (Ω)	C_{gb} (F)	α_{gb}	C_e (F)	α_e
Dark	303	200970	2.530E-11	0.915	2.667E6	3.181E-10	0.792	2.778E-7	0.599
	328	184550	3.044E-11	0.903	1.877E6	3.526E-10	0.791	5.054E-7	0.593
	353	135030	3.112E-11	0.903	1.021E6	3.528E-10	0.795	9.423E-7	0.559
	378	47264	8.893E-11	0.903	357550	1.007E-9	0.795	2.691E-6	0.559
Light	303	172850	2.943E-11	0.915	2.294E6	3.693E-10	0.792	3.241E-7	0.598



Figs. 5. (a) Nyquist plots of polycrystalline Cs_2AgSbI_6 measured in the dark over the temperature range 303–378 K, with inset comparison under dark and illuminated conditions at 303 K. (b) Arrhenius plots of grain and grain-boundary resistances extracted from impedance spectroscopy. (c) Bode plots of impedance magnitude and phase measured under dark and illuminated conditions at 303 K.

As shown in Fig. 5(c), the Bode representations which illustrate the frequency dependence of the impedance magnitude |Z| and phase at 303 K under dark and illuminated conditions provide further insight into the transport dynamics. Enhanced conductivity is confirmed by the impedance magnitude which is systematically reduced under illumination over the whole frequency range. However, two distinct relaxation regimes associated with bulk and grain-boundary processes are shown by the phase spectra which remain nearly unchanged between light and dark conditions. Illumination which modifies mainly the resistive components is demonstrated by this invariance of the phase response, while the characteristic time constants and the underlying relaxation mechanisms remain essentially unaffected. Such results not only confirm the coexistence of bulk and grain boundary-controlled transport in Cs_2AgSbI_6 but also provide strong experimental validation for the chosen equivalent circuit [57].

A quantitative and consistent picture of electrical transport in polycrystalline Cs_2AgSbI_6 is generally established by the impedance spectroscopy results. A transport regime governed by barrier-limited conduction and defect-assisted hopping is shown by the moderate but systematic photoconductive response, the thermally activated transport with activation energies in the range of 0.18–0.26 eV, the non-ideal capacitive behavior and the dominance of grain-boundary resistance. These findings completely agree with both the strong thermal quenching of photoluminescence and the large Urbach energy extracted from optical absorption, demonstrating a high density of localized states. Therefore, a robust experimental foundation for the SCAPS simulations presented in the following section where recombination and charge transport are modeled using defect-assisted SRH mechanisms constrained by experimentally-determined parameters is provided by the combined I–V and impedance results.

3.6. Defect-mediated charge transport and recombination : SCAPS-1D modeling

3.6.1. Device architecture and simulation framework

Using the SCAPS-1D software, numerical simulations were performed to identify the dominant loss mechanisms and to gain deeper insight into the experimentally-observed photovoltaic behavior [59, 60]. The experimentally investigated stack is faithfully reproduced by the simulated device architecture:

FTO / TiO_2 / Cs_2AgSbI_6 / Spiro-OMeTAD / metal contact (Fig. 6).

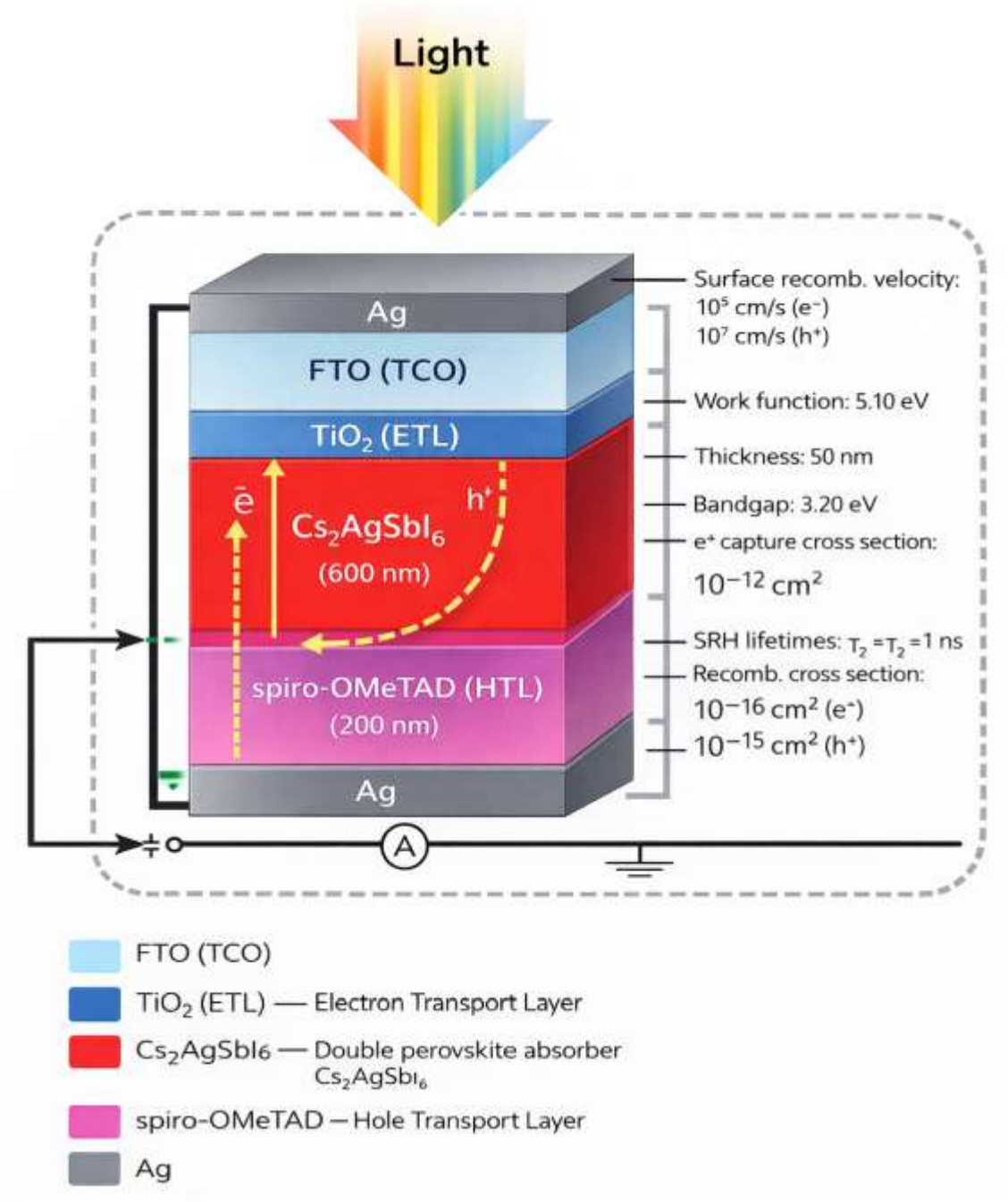


Fig. 6. Simulated device architecture used in SCAPS-1D: FTO/TiO_2/Cs_2AgSbI_6/Spiro-OMeTAD/metal contact.

All material parameters such as doping concentrations, carrier mobilities, dielectric permittivities, electron affinities and band gaps were selected in close consistency with not only previously-reported values for lead-free double perovskite systems but also experimental measurements [61-64]. At both electrodes, ohmic contacts were intentionally assumed so as to focus on interfacial recombination and intrinsic bulk processes. The fact that charge transport is limited by bulk recombination processes rather than by injection barriers is confirmed by the choice which is experimentally justified by the non-rectifying current-voltage and the quasi-linear characteristics observed in the dark. It should be noted that the SCAPS-1D simulations aim to translate experimentally-measured bulk recombination and transport

limitations into a device-level framework instead of reproducing an optimized experimental solar cell.

The self-consistent solution of Poisson's equation coupled with the steady-state continuity equations for holes and electrons describes the carrier transport in SCAPS-1D [65-67]:

$$\frac{d}{dx}\left(\varepsilon\frac{d\psi}{dx}\right) = -q\,(p - n + N_D^+ - N_A^- + \rho_{def}) \tag{14}$$

$$\frac{1}{q}\frac{dJ_n}{dx} + G - R = 0 \tag{15}$$

$$-\frac{1}{q}\frac{dJ_p}{dx} + G - R = 0 \tag{16}$$

where ψ represents the electrostatic potential, n and p are the electron and hole concentrations, G stands for the photogeneration rate and R refers to the total recombination rate.

It was assumed that the recombination mechanism was dominated primarily by the SRH recombination based on a strong experimental evidence pointing towards disorder-dominated recombination [68, 69], namely the ohmic-like transport behavior, the pronounced photoluminescence quenching and the large Urbach energy:

$$R_{SRH} = \frac{np - n_i^2}{\tau_p(n+n_1)+\tau_n(p+p_1)} \tag{17}$$

where the electron and hole lifetimes τ_n and τ_p are inversely proportional to the effective defect density N_t within the absorber layer.

Because of their negligible contribution under the present experimental conditions, radiative and Auger recombination channels were neglected as discussed below.

3.6.2. Simulated J–V characteristics and recombination-limited behavior

For different absorber defect densities, the simulated current–voltage (J–V) characteristics under AM1.5G illumination are displayed in Fig. 7. Characterized by fill factor, short-circuit current density (J_{sc}) and finite open-circuit voltage (V_{oc}), a clear photovoltaic response is obtained [70].

A progressive degradation of the J–V curves is observed since the effective defect density augments from 5×10^{18} to 1×10^{20} cm^{-3}. The probability of carrier collection is reduced and the carrier lifetime is shortened due to this evolution, which is physically consistent with enhanced SRH recombination. The pronounced curvature near open-circuit conditions does not reflect ideal diode behavior but rather reveal recombination-limited transport. This is in excellent agreement with the experimentally-observed non-rectifying I–V characteristics.

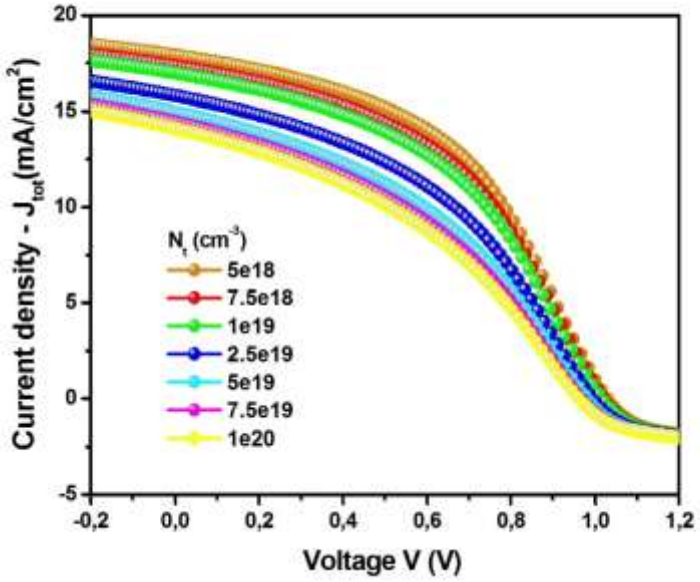


Fig. 7. Simulated J–V characteristics under AM1.5G illumination for different absorber defect densities.

3.6.3. Impact of absorber defect density on photovoltaic parameters

Fig. 8 and Table 3 provide a summary of the quantitative influence of the absorber defect density on the photovoltaic parameters. With increasing N_t, a monotonic decrease in power conversion efficiency, fill factor, V_{oc} and J_{sc} is observed, which is a hallmark of bulk-limited photovoltaic devices governed by nonradiative recombination.

The decrease in the quasi-Fermi level splitting can be directly related to the reduction in open-circuit voltage [71]:

$$qV_{oc} \approx E_{FN} - E_{FP} \tag{18}$$

V_{oc} is limited due to the enhanced nonradiative recombination which suppresses the separation between the electron and hole quasi-Fermi levels as the defect density augments. At the same time, because of the combined effects of recombination and series resistance, the fill factor degrades more moderately, while the short-circuit current density is lowered by the reduction in effective carrier lifetime.

Taking into consideration point defects added to grain-boundary-related states inherent to polycrystalline Cs_2AgSbI_6 and extended defects, it is important to emphasize that the relatively high defect density values used in the simulations (up to 1×10^{20} cm^{-3}) should be interpreted as an effective bulk defect density. These contributions are appropriately treated within SCAPS as an effective recombination center density and cannot be experimentally disentangled from a macroscopic device perspective. To capture recombination-limited transport regimes, similar effective defect densities have been widely adopted in numerical studies of emerging lead-free perovskite absorbers.

The performance limitations of Cs_2AgSbI_6 devices originate primarily from defect-mediated recombination, which is confirmed by the simulated trends that closely mirror the experimental observations.

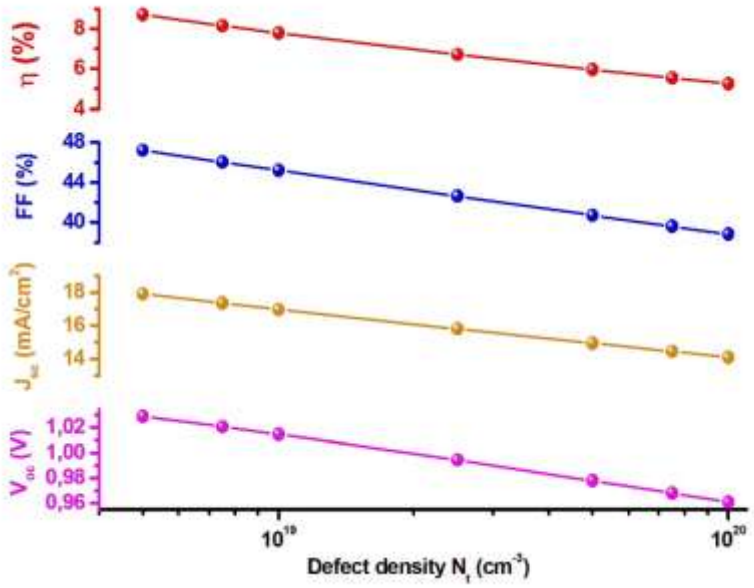


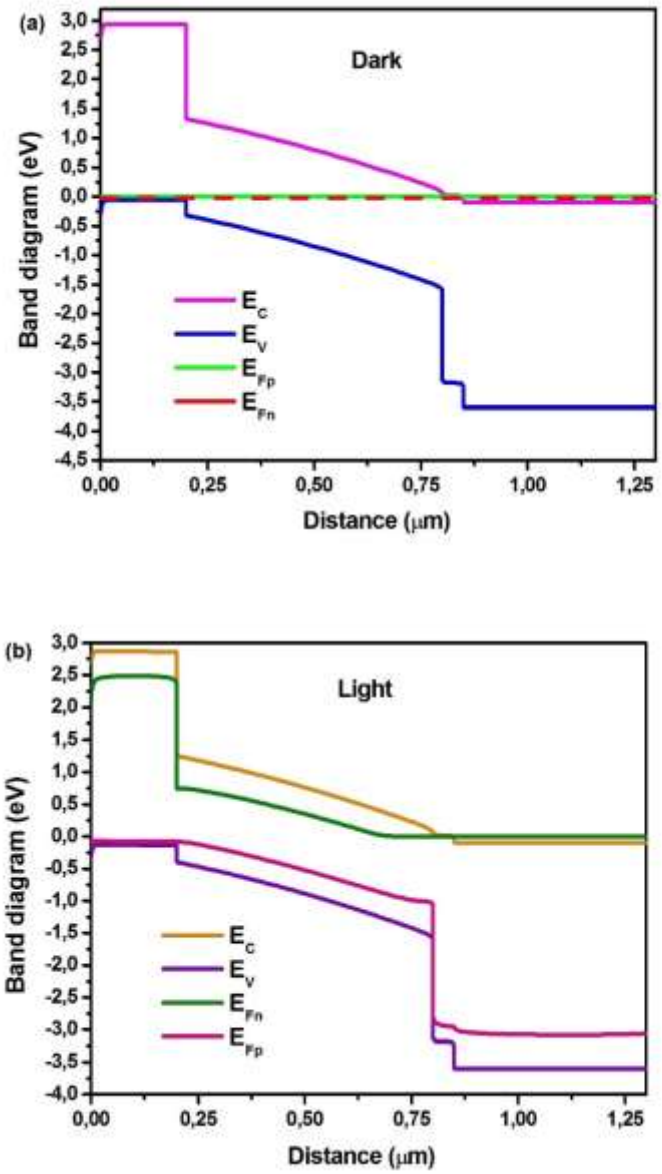
Fig. 8. Dependence of photovoltaic parameters on absorber defect density extracted from SCAPS-1D simulations.

Table 3. SCAPS-1D simulated photovoltaic parameters as a function of absorber defect density.

Nt (cm^{-3})	Voc (V)	Jsc (mA/cm^2)	FF (%)	Efficiency η (%)	V_{MPP} (V)	J_{MPP} (mA/cm^2)
5E18	1.028957	17.91516	47.201	8.701	0.676927	12.85366
7.5E18	1.020793	17.35651	46.0211	8.1538	0.667675	12.21216
1E19	1.014793	16.97041	45.2001	7.7841	0.661029	11.77574
2.5E19	0.994412	15.80275	42.6251	6.6983	0.635557	10.53925
5E19	0.977882	14.95263	40.7065	5.9521	0.614059	9.693001
7.5E19	0.967944	14.45245	39.5878	5.538	0.600829	9.217252
1E20	0.960733	14.09089	38.7998	5.2526	0.591687	8.877237

3.6.4. Energy band alignment and limited quasi-Fermi level splitting

Under dark and AM1.5G illuminated conditions, the simulated energy band diagrams for a representative high-defect case (Nt = 1 × 10^{20} cm^{-3}) are displayed in Figs. 9(a) and (b) respectively [72, 73]. Thermal equilibrium is demonstrated by the fact that the electron and hole quasi-Fermi levels under dark conditions coincide throughout the structure.



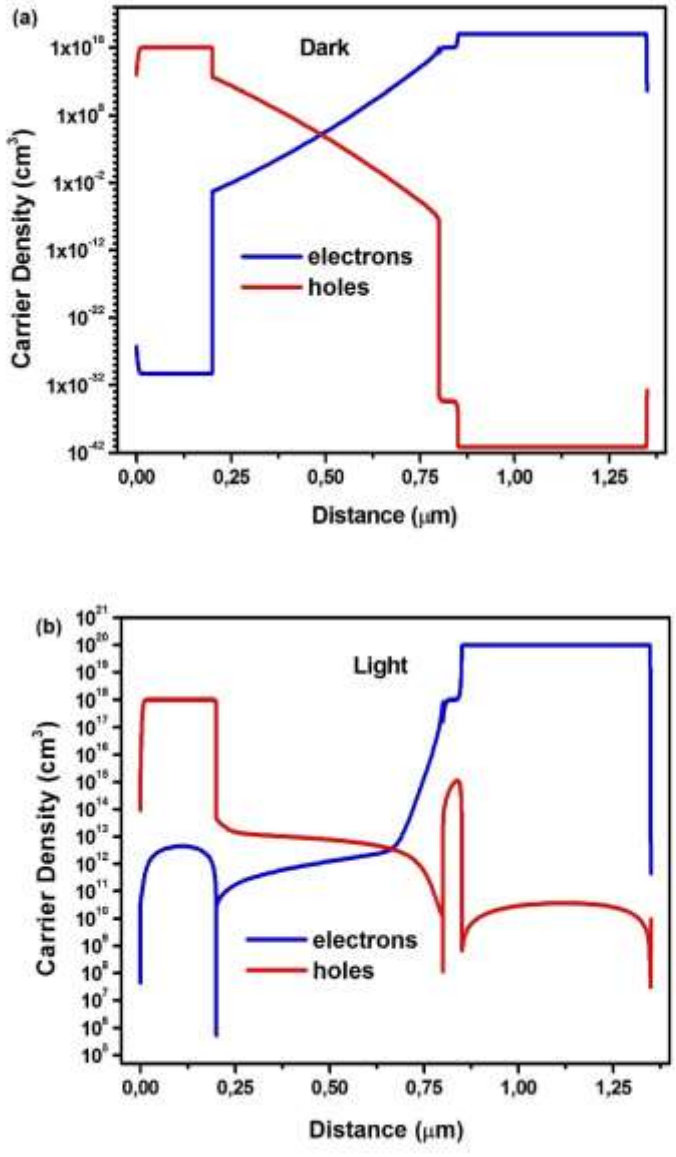
Figs. 9. Simulated energy band diagrams for a high-defect absorber (Nt = 1 × 10^{20} cm^{-3}) under (a) dark and (b) AM1.5G illuminated conditions.

A clear quasi-Fermi level splitting develops under illumination within the Cs_2AgSbI_6 absorber layer. Nevertheless, strong nonradiative recombination losses are confirmed by the magnitude of this splitting which remains limited. Such behavior is fully consistent with the strong thermal quenching observed experimentally and the weak photoluminescence intensity at room temperature.

Within the absorber, recombination not only limits the achievable photovoltage but also prevents significant carrier accumulation even though favorable band bending at the TiO_2/Cs_2AgSbI_6 and Cs_2AgSbI_6/Spiro-OMeTAD interfaces facilitates charge extraction.

3.6.5. Spatial carrier density profiles under dark and illuminated conditions

Under dark and AM1.5G illuminated conditions, the spatial distributions of electron and hole concentrations are shown in Figs. 10(a) and (b) respectively [74]. The absence of strong built-in junction behavior is confirmed by the carrier concentrations which remain close to their equilibrium values in the dark.



Figs. 10. Spatial distributions of electron and hole concentrations under (a) dark and (b) AM1.5G illuminated conditions.

There is no pronounced carrier accumulation although moderate increases in carrier densities under illumination are observed within the absorber layer. Such behavior agrees with the short

effective lifetimes imposed by high defect density as it indicates rapid recombination of photogenerated carriers. The absence of significant carrier pile-up further confirms that transport is not governed by space-charge-limited effects or injection barriers. It is rather dominated by distributed bulk recombination.

3.6.6. Spatial profiles of photogeneration and SRH recombination

The spatial profiles of SRH recombination rates and photogeneration across the device thickness are shown in Fig. 11. As expected from its absorption characteristics, the photogeneration rate peaks within the Cs_2AgSbI_6 absorber. However, the SRH recombination rate reaches its maximum within the same region as it follows a comparable spatial distribution [75].

A substantial fraction of photogenerated carriers which recombine before extraction is proven by this strong spatial overlap. Throughout the structure, radiative recombination remains negligible, which is consistent with the extremely weak photoluminescence observed experimentally. Such results provide direct numerical confirmation that defect-mediated SRH recombination not only limits device performance but also governs carrier losses.

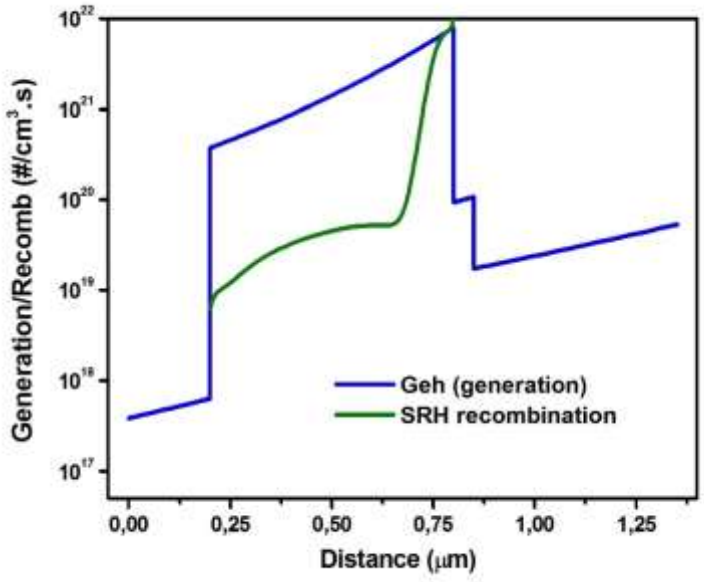


Fig. 11. Spatial profiles of photogeneration and Shockley–Read–Hall recombination rates across the device thickness.

3.6.7. Correlation between experimental observations and SCAPS simulations

The strong and physically-consistent correlation between the SCAPS-1D simulations and the experimental observations is the central outcome of this paper. Within a defect-controlled SRH recombination framework, the moderate photocurrent enhancement under illumination,

the ohmic-like current–voltage characteristics, the pronounced photoluminescence (PL) quenching and the large Urbach energy are all coherently reproduced. Such agreement confirms that charge carrier losses in Cs_2AgSbI_6 are predominantly dominated by nonradiative recombination mediated by a high density of electronic defects.

In particular, a common physical origin associated with shallow disorder-induced states near the band edges is strongly indicated by the close correspondence between the Urbach energy (≈ 90 meV) and the activation energy extracted from temperature-dependent PL quenching (≈ 85 meV). SRH recombination channels which naturally result in suppressed radiative efficiency, limited quasi-Fermi level splitting and reduced carrier lifetimes explicitly take into consideration these defect states within the SCAPS formalism. Thus, both the current density and the simulated open-circuit voltage remain intrinsically constrained, which is consistent with not only the non-ideal transport behavior but also the experimentally observed weak PL emission.

More importantly, the SCAPS-1D simulations provide a physics-based framework that translates transport limitations and experimentally-measured bulk recombination into a device-level description rather than reproduce a fully realized or optimized experimental solar cell. The simulations capture the intrinsic performance ceiling imposed by the material quality instead of an idealized device scenario by incorporating recombination parameters and defect densities which are consistent with electrical, optical and photoluminescence measurements.

The SCAPS results should not, therefore, be interpreted as a prediction of achievable device efficiency but rather as a quantitative extension of the experimentally observed recombination-limited behavior. Indeed, the simulations serve not only to delineate the material-level bottlenecks currently limiting photovoltaic performance but also to identify the dominant loss mechanisms. Such findings clearly demonstrate that, through optimized interface engineering, targeted passivation strategies or enhanced crystallinity, the most critical pathway towards unlocking higher efficiencies in Cs_2AgSbI_6-based optoelectronic devices proves to be reducing bulk and interfacial defect densities.

4. Conclusion and Outlook

The combined numerical and experimental investigation of both charge transport and defect-mediated recombination in lead-free Cs_2AgSbI_6 double perovskites has been the focus of our paper. A highly disordered electronic structure characterized by dominant nonradiative recombination pathways and a large Urbach energy is consistently pointed out by electrical transport measurements, temperature-dependent photoluminescence and optical spectroscopy.

Charge-carrier dynamics in Cs_2AgSbI_6, based on these results, are intrinsically limited by defect-related states located near the band edges.

These material-level limitations are translated into a device-level framework through SCAPS-1D simulations implemented using experimentally-relevant material parameters. The SRH recombination is identified as the primary mechanism restricting photovoltaic performance and quasi-Fermi level splitting by the numerical analysis. Thus, this offers a physically-grounded explanation for the carrier collection efficiency and the limited open-circuit voltage associated with this material system. It should be noted that the simulations are found to elucidate how experimentally-observed recombination losses propagate into photovoltaic metrics instead of predicting optimized device efficiencies.

From an forward-looking perspective, suppressing defect-assisted nonradiative recombination at the interface and bulk levels will be critically necessary for more development in Cs_2AgSbI_6-based optoelectronic devices as indicated by the present findings. Hence, future efforts ought to prioritize (i) optimizing interfacial band alignment to decrease recombination losses and carrier trapping, (ii) enhancing film crystallinity so as to minimize structural disorder and (iii) implementing targeted chemical passivation strategies in order to deactivate shallow defect states. This study offers a realistic framework to guide future device design and material optimization towards viable lead-free perovskite solar cells by establishing a quantitative and direct connection between device-level limitations, recombination physics and experimentally-observed disorder.

Data Availability

The datasets generated and/or analyzed during the current study are available in the Zenodo repository, https://zenodo.org/records/19319156.

References

[1] R. Yang, D. Yang, S.F. Liu, Chemical Reviews 126 (2026) 1408–1469.

[2] B. Li, D. Wang, Y. Hou, F. Liu, B. Du, L. Wang, Journal of Materials Chemistry C 14 (2025) 969–988.

[3] J. Thiesbrummel, J.V. Milić, C. Deibel, E.C. Garnett, S. Tao, T. Kirchartz, A. Guerrero, P. Cameron, W. Tress, M.S. Islam, B. Ehrler, Nature Reviews Chemistry (2026).

[4] L. Ebrahimkhani, V. Mirkhani, M. Moghadam, S. Tangestaninejad, A.H. Montazer, M. Ebrahimkhani, I.M. Poor-Baltork, Optical and Quantum Electronics 58 (2026).

[5] N. Bansal, S. Porwal, P. Singh, T. Singh, in: Elsevier eBooks, 2025, pp. 313–355.

[6] S.S. Shin, B.-W. Park, J.H. Noh, S.I. Seok, Nature Photonics 20 (2026) 11–23.

[7] T. Kimura, N. Oshita, K. Sato, A. Masuhara, T. Chiba, Journal of Materials Chemistry C 14 (2026) 1291–1307.

[8] Y. Zhang, G. Fu, Z. Liang, S. Liu, N. Park, Advanced Energy Materials (2026).

[9] N. Mondal, A. Samanta, Chemical Communications 62 (2025) 738–751.

[10] B.T. Ayalew, S.G. Kuma, Advances in Condensed Matter Physics 2026 (2026).

[11] K. Markopoulos, F. Bairamis, G. Zardalidis, K. Brintakis, A. Kostopoulou, G. Kioseoglou, E. Stratakis, F. Farmakis, Advanced Materials Technologies (2026).

[12] M.K.M. Ali, A.A. Mohsen, N.K. Allam, Solar Energy Materials and Solar Cells 295 (2025) 114025.

[13] R. Zhu, X. Ge, G. Feng, A. Wang, X.-C. Hang, L. Ruan, Z. Deng, W. Huang, Chemical Society Reviews 55 (2025) 1039–1088.

[14] J.M. Fernandes, S. Dutta, Small 22 (2025) e09737.

[15] R. Mastria, H.T. Lam, I. Leontis, S. Bonomi, M.A.S. Alshehri, A. Rizzo, P. Galinetto, M. Patrini, N. Taylor, S.P. Hepplestone, M.F. Craciun, L. Malavasi, S. Russo, Advanced Science (2026) e17469.

[16] I. Poli, T. Gatti, Y. Li, A. Agresti, L.A. Castriotta, F. De Rossi, S. Shukla, T. Aernouts, S. Eslava, L. Malavasi, E. Mosconi, J. Van Embden, D. Kalita, E. Della Gaspera, G.K. Grandhi, K. Mokurala, P. Vivo, N.K. Noel, J.B. Patel, M. Righetto, P. Ragonese, S. Ravishankar, C. Maurizio, F. Lamberti, K.P.S. Zanoni, M. Sessolo, M. Morales-Masis, R. Bhatia, S. Argiolas, A.L. Donne, A. Mattoni, S. Meloni, J. Baker, R. Vidal, Journal of Physics Energy 8 (2025) 011501.

[17] A. Ali, B. Anissa, D. Radouan, N.A. Bouzieh, N. Amrane, Modern Physics Letters B 39 (2025).

[18] M.J. Hossen, H.M. Hamzah, M. Shahinuzzaman, Jamal, S.M. Said, S.F.W.M. Hatta, M.H. Miah, M.U. Khandaker, M.A. Islam, Physica Scripta 100 (2024) 012005.

[19] M. Abdellaoui, R. Touti, A.E. Mekkaouy, E.H. Akarchaou, L. Talha, A. Tahiri, M. Filali, S. Chtita, Next Materials 10 (2025) 101548.

[20] A.S. Aljaloud, A. Jebnouni, A.F. Alshammari, A.A. AlDheirib, M.A.F. Alshammari, T. Alkathiri, M. Bouzidi, M.B. Bechir, Optical Materials 166 (2025) 117172.

[21] A.M. Jafar, K.A. Khalaph, A.M. Hmood, N.Kh. Abdalameera, AIP Conference Proceedings 2834 (2023) 090031.

[22] N. Israr, W.U. Rehman, M.A. Jehangir, N.S.A. El-Gawaad, U. Farooq, Journal of Inorganic and Organometallic Polymers and Materials 35 (2025) 8429–8444.

[23] A. Sajjad, M. Faizan, T.A. Alrebdi, G. Murtaza, J. Rehman, X. Shen, Y. Dong, K. Shaheen, S.H. Khan, Physical Chemistry Chemical Physics 27 (2025) 4880–4891.

[24] M. Alla, O.P. Mishra, G.R. Wakale, E. Choudhary, V. Manjunath, M.K. Hossain, M. Rouchdi, B. Fares, Advanced Theory and Simulations 7 (2023).

[25] F. Horani, D.R. Gamelin, Journal of the American Chemical Society 147 (2025) 16552–16559.

[26] M.N. Nahid, M.S. Shah, H. Mamur, R. Hosen, M.R.A. Bhuiyan, Chemistry of Inorganic Materials 4 (2024) 100069.

[27] M. Shirazi, Journal of Optics (2025).

[28] M.K. Hossain, S. Islam, M.N. Sakib, M.S. Uddin, G.F.I. Toki, M.H.K. Rubel, J. Nasrin, S.H. Shahatha, M.R. Mohammad, A.A. Alothman, C.J. Raorane, R. Haldhar, H. Bencherif, Advanced Electronic Materials 11 (2024).

[29] K.I.F. Utsho, S.M.G. Mostafa, Md. Tarekuzzaman, M.S.M. Al-Saleem, N.I. Nahid, J.Y. Al-Humaidi, Md. Rasheduzzaman, M.M. Rahman, Md.Z. Hasan, RSC Advances 15 (2025) 2184–2204.

[30] J. Hakami, Results in Engineering 25 (2025) 104044.

[31] M.B. Bechir, F. Alresheedi, RSC Advances 14 (2024) 1634–1648.

[32] M.B. Bechir, F. Alresheedi, Physical Chemistry Chemical Physics 26 (2023) 1274–1283.

[33] W. Hallab, H. Wahbi, R. Msalmi, N. Mhadhbi, F. Saadi, F. Aouaini, B. Basha, A. Sánchez-Coronilla, H. Naïli, Journal of Materials Science Materials in Electronics 36 (2025).

[34] M.B. Bechir, M.B. Bechir, M.H. Dhaou, M.H. Dhaou, S.M. Altrifi, Materials Research Bulletin 167 (2023) 112381.

[35] D.R. Almalawi, M. Bouzidi, I.H. Smaili, N.I. Aljuraide, A. Alzahrani, A. Saftah, D. Alzahrani, M.B. Bechir, Journal of Materials Science Materials in Electronics 36 (2025).

[36] R. Balakrishnan, P. Sahoo, B. Karuppannan, A. Dixit, Physica Scripta 100 (2025) 105969.

[37] F. Ebadi, K. Meraji, M. a. T. Cachafeiro, F. Wolf, M.T. Sirtl, T. Bein, W. Tress, Advanced Energy Materials 15 (2025).

[38] M. Yang, W. Ge, Y. Guo, J. Li, Y. Li, Journal of Alloys and Compounds 1032 (2025) 181218.

[39] H. Suo, N. Wang, Y. Zhang, X. Zhang, J. Xiang, X. Wang, G. Xing, D. Guo, J. Chang, Y. Wang, P. Li, Z. Wang, Y. Zhang, B. Chen, S. Li, C. Guo, F. Wang, Light Science & Applications 14 (2025) 21.

[40] H. Wang, J. Yao, Z. Yin, S. Cao, J. Zhao, X. Han, W.W. Yu, R. Zeng, Laser & Photonics Review 19 (2025).

[41] A.B.C. Kameni, A. Py-Renaudie, D. Garrot, B. Berenguier, G. Bouchez, D.R. Ceratti, P. Schulz, J. Guillemoles, G. Delport, Advanced Optical Materials 13 (2025).

[42] W. Ma, X. Ren, J. Wang, X. Tan, M. Cui, K. Liu, H. Ren, J. Liu, H. Wang, X. Xi, S. Bi, ACS Applied Materials & Interfaces 17 (2025) 58973–58982.

[43] S. Qu, Y. Li, H. Huang, F. Yang, C. Sun, Q. Zhang, Z. Wang, T. Jiang, L. Yan, Z. Lan, Y. Yang, P. Cui, X. Ai, M. Li, Advanced Materials 37 (2025) e2508643.

[44] M. Cao, Y. Dong, S. Liu, Journal of Physics Conference Series 2966 (2025) 012015.

[45] P. Li, T.J. Kools, H. Pezeshki, J.M.B.E. Joosten, J. Li, J. Igarashi, J. Hohlfeld, R. Lavrijsen, S. Mangin, G. Malinowski, B. Koopmans, Physical Review. B./Physical Review. B 111 (2025).

[46] M.B. Coban, A.S. Altowyan, U.H. Kaynar, J. Hakami, H. Aydin, I. Kara, A. Canimoglu, N. Can, Ceramics International (2026).

[47] A. Bakytkyzy, Z.T. Karipbayev, A. Dauletbekova, A.M. Zhunusbekov, M. Kemere, M. Konuhova, A. Sarakovskis, A.I. Popov, Crystals 15 (2025) 909.

[48] H. Cheng, Y. Feng, Y. Fu, Y. Zheng, Y. Shao, Y. Bai, Journal of Materials Chemistry C 10 (2022) 13590–13610.

[49] T. Handa, T. Aharen, A. Wakamiya, Y. Kanemitsu, Physical Review Materials 2 (2018).

[50] B.K. Jones, J. Santana, M. McPherson, Solid State Communications 105 (1998) 547–549.

[51] X. Guan, W. Hu, M.A. Haque, N. Wei, Z. Liu, A. Chen, T. Wu, Advanced Functional Materials 28 (2017).

[52] M.K. Thakan, M. Khemnani, J. Gosai, A. Solanki, V. Kheraj, ACS Applied Materials & Interfaces 17 (2025) 57343–57354.

[53] I. Jahan, J.D. Arellano, Z. Shi, Journal of Materials Chemistry C 13 (2025) 23675–23695.

[54] X.-Z. Hu, J. Li, H.-Z. Ji, Q.-F. Ren, X.-M. Luo, S.-Q. Zang, Nano Research 19 (2025) 94907805.

[55] F. Greuter, G. Blatter, Semiconductor Science and Technology 5 (1990) 111–137.

[56] Md. Tarekuzzaman, K.I.F. Utsho, A.S. Sarker, Md.I.U. Forkan, Md.A. Khan, ACS Applied Energy Materials 8 (2025) 15961–15992.

[57] M. Bouzidi, D.R. Almalawi, I.H. Smaili, N.I. Aljuraide, A. Alzahrani, A. Saftah, M.B. Bechir, Solid State Sciences 170 (2025) 108134.

[58] D.R. Almalawi, M. Bouzidi, I.H. Smaili, N.I. Aljuraide, A. Alzahrani, A. Saftah, M.B. Bechir, Scientific Reports 15 (2025) 26807.

[59] R. Kundara, S. Baghel, Solar Energy 287 (2025) 113253.

[60] V.H.D. Araújo, A.F. Nogueira, J.C. Tristão, L.J.D. Santos, RSC Sustainability 3 (2025) 4314–4335.

[61] K. Fatema, M. Shawon, Materials Research Express 13 (2025) 016403.

[62] S.E. Boussaada, Y. Mouchaal, H. Riane, A. Khelil, Optical and Quantum Electronics 57 (2025).

[63] P.K. Moone, N. Sharifi, Journal of Optics (2024).

[64] N.R. Pochont, Y.R. Sekhar, Inorganics 11 (2022) 3.

[65] W. Zulhafizhazuan, K. Sobayel, S. Shafian, S. Sepeai, M.A. Ibrahim, Interactions 246 (2025).

[66] W. Luqman, M. Aamir, M.N. Sharif, M. Sher, M.E. Khan, Q. Wali, H. Almohamadi, Md. Akhtaruzzaman, T. Taima, J.-M. Nunzi, Md. Shahiduzzaman, The European Physical Journal Applied Physics 100 (2025) 25.

[67] M.K. Hossain, M.K.A. Mohammed, R. Pandey, A.A. Arnab, M.H.K. Rubel, K.M. Hossain, M.H. Ali, Md.F. Rahman, H. Bencherif, J. Madan, Md.R. Islam, D.P. Samajdar, S. Bhattarai, Energy & Fuels 37 (2023) 6078–6098.

[68] S. Rabhi, K. Sekar, K. Kalna, Y.I. Bouderbala, N. Bouri, N. Oueldna, N. Belbachir, K. Dadda, M.S. Aida, N. Attaf, Optical and Quantum Electronics 56 (2024).

[69] T.O. Ahmed, T.T. Ibrahim, E.O. Oladimeji, J.D. Koffa, Brazilian Journal of Physics 54 (2024).

[70] A.M. Houmomou, S. Mohammadou, G.M.D. Kenfack, F.T. Nya, A. Laref, A. Mohamadou, Energy Technology 11 (2023).

[71] M.U. Salman, M. Mehak, U. Ali, G.M.U. Din, S.M. Ramay, M. Younis, S. Atiq, RSC Advances 15 (2025) 15618–15629.

[72] A. Lafuente-Sampietro, K. Yoshida, S. Wang, S. Ishizuka, H. Shibata, N. Sano, K. Akimoto, T. Sakurai, Solar Energy Materials and Solar Cells 223 (2021) 110948.

[73] A. Ghosh, S.S. Dipta, S.S.S. Nikor, N. Saqib, A. Saha, Journal of the Optical Society of America B 37 (2020) 1966.

[74] Md. Tarekuzzaman, Md.H. Ishraq, A.S. Sarker, Md.Z. Hasan, S.S. Hasan, Journal of Materials Science 61 (2025) 960–1002.

[75] E.L. Meyer, S.A. Mvokwe, O.O. Oyedeji, N. Rono, M.A. Agoro, Materials 18 (2025) 186.

Acknowledgments

The authors extend their appreciation to Northern Border University, Saudi Arabia, for supporting this work through project number (NBU-CRP-2026-2461).

Author contributions

Mohamed Bouzidi: Conceptualization; Methodology; Investigation; Formal analysis; Data curation; Visualization; Writing – original draft; Numerical simulation using SCAPS-1D. Abdullah A. Alatawi: Optical measurements; Photoluminescence analysis; Data interpretation; Review & editing of the manuscript. Turki Alkathiri: Electrical measurements; Impedance spectroscopy analysis; Data processing; Validation. Sultan Albarakati: Experimental support; Structural characterization; Assistance in measurements. Norah Alwadai: Optical characterization; Data analysis; Visualization. Ahmed F. Almutairi: Electrical transport measurements; I–V characterization; Data analysis. Refka Ghodhbani: Methodological support; Scientific discussion; Validation of results. Mohamed Ben Bechir: Supervision; Scientific oversight.

Funding: This research has been funded by Scientific Research Deanship at Northern Border University, Saudi Arabia through project number (NBU-CRP-2026-2461).

Competing interests

The authors declare no competing interests.

Correspondence and requests for materials should be addressed to Mohamed Ben Bechir

Figure Legends

Figs. 1. (a) X-ray diffraction pattern of polycrystalline Cs_2AgSbI_6 recorded at room temperature. (b) Crystal structure of cubic Cs_2AgSbI_6 visualized using VESTA software.

Figs. 2. (a) UV–visible diffuse reflectance spectrum of polycrystalline Cs_2AgSbI_6. (b) Tauc plot for the indirect allowed transition derived from the Kubelka–Munk function. (c) Tauc plot for the direct allowed transition at higher photon energies. (d) Urbach plot extracted from diffuse reflectance data for the determination of the Urbach energy.

Figs. 3. (a) Steady-state photoluminescence spectra of polycrystalline Cs_2AgSbI_6 recorded over the temperature range 70–300 K. (b) Temperature dependence of the integrated photoluminescence intensity. (c) Temperature dependence of photoluminescence peak energy and full width at half maximum. (d) Photoluminescence spectra under illumination and dark conditions at room temperature.

Figs. 4. (a) Current–voltage characteristics of polycrystalline Cs_2AgSbI_6 measured under dark and illuminated conditions at room temperature. (b) Low-bias current–voltage response and linear fitting of the ohmic regime.

Figs. 5. (a) Nyquist plots of polycrystalline Cs_2AgSbI_6 measured in the dark over the temperature range 303–378 K, with inset comparison under dark and illuminated conditions at 303 K. (b) Arrhenius plots of grain and grain-boundary resistances extracted from impedance spectroscopy. (c) Bode plots of impedance magnitude and phase measured under dark and illuminated conditions at 303 K.

Fig. 6. Simulated device architecture used in SCAPS-1D: FTO/TiO_2/Cs_2AgSbI_6/Spiro-OMeTAD/metal contact.

Fig. 7. Simulated J–V characteristics under AM1.5G illumination for different absorber defect densities.

Fig. 8. Dependence of photovoltaic parameters on absorber defect density extracted from SCAPS-1D simulations.

Figs. 9. Simulated energy band diagrams for a high-defect absorber ($N_t = 1 \times 10^{20}$ cm^{-3}) under (a) dark and (b) AM1.5G illuminated conditions.

Figs. 10. Spatial distributions of electron and hole concentrations under (a) dark and (b) AM1.5G illuminated conditions.

Fig. 11. Spatial profiles of photogeneration and Shockley–Read–Hall recombination rates across the device thickness.

Supplementary Files

This is a list of supplementary files associated with this preprint. Click to download.

- SupportingInformation.pdf